Research Square

Preprints are preliminary reports that have not undergone peer review.
They should not be considered conclusive, used to inform clinical practice,
or referenced by the media as validated information.

The Co(II) ion binds to the N-terminal region of amyloid-beta (Aβ) peptides and modulates Aβ aggregation

Sebastian K.T.S. Wärmländer

seb@student.su.se

Stockholm University

Elina Berntsson

Stockholm University

Merlin Sardis

Tallinn University of Technology

Jonathan Pansieri

Umeå University

Xiaolin Dong

Stockholm University

Jüri Jarvet

Stockholm University

Vello Tõugu

Tallinn University of Technology

Ludmilla Morozova-Roche

Umeå University

Per M. Roos

Karolinska Institutet

Peep Palumaa

Tallinn University of Technology

Astrid Gräslund

Stockholm University

Research Article

Keywords: Alzheimer's disease, amyloid, cobalt, protein-metal binding, protein aggregation

Posted Date: April 1st, 2026

DOI: https://doi.org/10.21203/rs.3.rs-9246550/v1

License: This work is licensed under a Creative Commons Attribution 4.0 International License.
Read Full License

Additional Declarations: The authors declare potential competing interests as follows: Authors J.P., L.M.-R., M.S., P.R., P.P., V.T. and X.D. have no conflicts of interest to disclose. A.G., E.B., J.J., and S.W. are shareholders in CellPept Sweden AB. Neither this company, nor the funding organizations, had any role in the design of the study; in the collection, analyses, or interpretation of data; in the writing of the manuscript; or in the decision to publish the results.

Abstract

Aggregating amyloid-β (Aβ) peptides play a central role in the neuropathology of Alzheimer's disease (AD), the leading cause of dementia worldwide. In AD brains, Aβ peptides aggregate into insoluble amyloid plaques that contain elevated metal concentrations. AD patients furthermore often exhibit disrupted metal homeostasis. Despite extensive investigation, the metal aspect of AD remains unclear. Despite being an essential trace element with well-documented toxic properties, cobalt (Co) has received little attention in AD research.

Here, we demonstrate for the first time that Co(II) ions bind to the N-terminal region of the biologically relevant full-length $A\beta_{40}$ peptide. The His6, His13, and His14 residues participate in metal coordination. The binding affinity of the Co(II)·$A\beta_{40}$ complex is relatively weak and estimated to around 0.3 mM. Thus, as expected, Aβ binding to Co(II) is weaker than to Cu(II), Ni(II), and Zn(II), but also weaker than Mn(II) binding, which is not consistent with the Irving–Williams series.

Equimolar concentrations of Co(II) were found to disrupt normal Aβ40 fibrillation, primarily by interfering with fibril elongation. Co(II) also induced structural rearrangements—specifically coil–coil interactions—in $A\beta_{40}$ monomers positioned in membrane-mimicking SDS micelles. These structural effects may influence the harmful Aβ aggregation processes underlying AD. More broadly, inducing protein misfolding and aggregation could be a general mechanism of cobalt toxicity.

1. Introduction

AD is a progressive, irreversible, and currently incurable chronic neurodegenerative disorder, and also the leading cause of dementia worldwide [1, 2]. Pathological hallmarks of AD include brain atrophy, with extensive deposits of amyloid plaques and neurofibrillary Tau tangles occurring years before the manifestation of disease symptoms [1, 2]. The insoluble plaques consist mainly of amyloid-β (Aβ) peptides [3] aggregated into fibrils that display a characteristic cross-β structure [4]. The plaques, which in AD brains contain elevated metal concentrations [5], are the end-product of an aggregation process [6–8] that involves formation of extra- and intracellular intermediates such as soluble neurotoxic Aβ oligomers [9]. As the latter are considered one of the main toxic species in AD brains [10], it becomes imperative to investigate factors that may influence Aβ aggregation and oligomer formation [11].

The Aβ peptides are intrinsically disordered in monomeric form and soluble in water [12]. The central and C-terminal Aβ segments are hydrophobic and can interact with membranes or fold into a hairpin conformation that likely is required for aggregation [13], while the anionic N-terminal segment is hydrophilic and readily interacts with cations including metal ions [12, 14]. As many different metal ions have been shown to bind to Aβ peptides and modulate their aggregation [14–17], as the amyloid plaques in AD brains contain elevated metal concentrations of e.g. Cu, Co, Fe, Tn, and Zn [5, 18, 19], and as AD patients typically display disrupted metal homeostasis [20–23], it becomes important to investigate the metal aspect of AD neuropathology [12, 20, 21].

Cobalt (Co) is an essential trace metal that has received relatively little attention in AD research, despite its well-documented toxic properties [24]. Elevated Co concentrations have been found in AD blood [25] and in AD serum [26], and Co nanoparticles have been linked to AD and to neurodegeneration in general [27, 28]. Thus, Co may affect the molecular mechanisms in AD pathology [29], and some cobalt complexes have been shown to modulate Aβ aggregation [30–33]. Co(II) ions have been reported to bind to Aβ peptide fragments [34, 35], but no studies have so far investigated the molecular interactions between Co ions and biologically relevant, full-length Aβ peptides.

In this study, we use transmission electron microscopy (TEM) imaging together with fluorescence, circular dichroism (CD) and nuclear magnetic resonance (NMR) spectroscopy to study *in vitro* interactions between Aβ peptides and Co(II) ions. The focus is to characterize the properties of Co(II) binding and its effects on Aβ structure and aggregation. Comparing Co(II) binding to wildtype Aβ(1–40), i.e., $A\beta_{40}$, and the Aβ(1–40)(H6A, H13A, H14A) mutant, i.e., $A\beta_{NoHis}$, allowed us to investigate the importance of the three N-terminal His residues for interactions with Co(II).

2. Cobalt exposure and toxicity

Biologically, cobalt (Co) is an essential element involved as a key component in several enzymes [36], in metabolic co-factors such as cobalamin (vitamin B12), and in biological processes such as myelin synthesis, metabolism of fatty- and amino acids, and DNA synthesis [37, 38]. However, only trace amounts of Co are needed for these tasks. In abundance, Co has toxic effects [39, 40].

Even though Co intoxication is generally uncommon, it may occur from either chronic or acute exposure [41]. After uptake, most Co is excreted via urine and therefore does not accumulate in the organism [42, 43]. Thus, the Co concentration in urine and/or blood can be used as a biomarker of Co exposure [44, 45]. One study reported the Co concentration in CSF to be around 15% of that in blood [46], suggesting a barrier mechanism. Furthermore, Co accumulation patterns in exposed rodents suggest that the choroid plexus might function as an absorptive barrier [47].

Co has multiple uses in modern industry, mainly due to its ferromagnetic and corrosion-resistant properties, and the industrial use of Co is expected to increase in the coming decades [48]. Currently, Co is used in batteries, dyes, magnets, cooling oils, dental materials, and in alloys of iron or carbides [49]. Many cancer treatments with external gamma rays still employ radioactive ^{60}Co as the source of radiation [50]. In addition, Co is common in orthopedic implants, leading to release of Co ions and Co nanoparticles into surrounding tissues [46, 51–53], which may cause Co intoxication [54–59]. With these different uses, human Co exposure is slowly increasing [60].

The symptoms and effects of Co intoxication vary depending on exposure route and chemical form of Co [61]. For example, the International Agency for Research on Cancer (IARC) classify cobalt sulfate and cobalt chloride as carcinogenic, and the composite alloy tungsten carbide-cobalt (WC-Co) is considered “probably carcinogenic to humans” [62]. In industries where workers are exposed to dust and fumes

contaminated with cobalt particles, adverse effects are typically observed in the respiratory system (asthma, fibrosis alveolitis and lung cancer) and in the skin (dermatitis) [61, 63, 64].

The details of cobalt toxicity are not fully understood, but a major toxic species might be free (non-bound) Co ions [65, 66]. Co ions exist in different oxidation states, where Co(II) is the most stable [67]. As Co(II) can both be reduced to Co(I) and oxidized to Co(III) or Co(IV), Co(II) is very redox-active and readily generates harmful reactive oxygen species (ROS) via Fenton-like reactions [68]. In addition to inducing oxidative damage [69, 70], Co(II) ions may also replace biologically useful divalent ions such as Ca(II) and Zn(II) [52, 71, 72]. In the circulatory system, Co(II) ions are typically transported by plasma proteins such as human serum albumin (HSA), lipoproteins, transferrin and haptoglobin [73, 74]. Because they reduce the amount of free Co ions, these proteins appear to have a protective effect against Co toxicity.

A possible connection between Co and neurodegeneration remains to be established. Some case studies have reported neurotoxic effects after Co exposure [40, 75–77]. In patients with amyotrophic lateral sclerosis (ALS), Co in cerebrospinal fluid was higher than in healthy controls in 18% of ALS cases [78]. In ALS liver samples Co concentrations were 78.4 ng/g, in contrast to 45.2 ng/g in healthy controls ($p < 0.05$) [79]. In an ALS motor neuron-like cell line, exposure to Co chloride evoked signs of oxidative toxicity associated with motor neuron death as in ALS [80]. Studies of neuronal SHSY5Y cells [76], mice [81], and nematodes [28] have shown that ROS damage and deposition of Aβ increases upon exposure to Co(II) ions and Co nanoparticles, respectively. Yet, the increased concentrations of Co and other metals in blood due to medical implants do not show clear correlations with e.g. AD pathology [82, 83].

3. Materials and methods

3.1 Materials and sample preparation

MES (2-[N-morpholino] ethane sulfonic acid) buffer, thioflavin-T (ThT) dye, sodium phosphate buffer, sodium dodecyl sulphate (SDS) detergent, (1,1,1,3,3,3)-hexafluoroisopropanol (HFIP) solvent, and salts of NaOH, NH_4OH, $CoCl_2 \bullet 6H_2O$ and $Cu(OAc)_2$ were all purchased from Sigma Aldrich (USA).

Recombinant wild-type $A\beta_{40}$ peptide (both unlabeled and uniformly ^{15}N-labelled) with the primary sequence $DAEFR_5HDSGY_{10}EVHHQ_{15}KLVFF_{20}AEDVG_{25}SNKGA_{30}IIGLM_{35}VGGVV_{40}$, and the recombinant $A\beta_{40}$ triple-histidine mutant $A\beta_{40}$(H6A, H13A, H14A), abbreviated $A\beta_{NoHis}$, were purchased as lyophilized powder from Alexotech AB (Umeå, Sweden). For the fluorescence spectroscopy measurements, lyophilized recombinant $A\beta_{40}$ powder was purchased from rPeptide LLC (Bogart, GA, USA).

All peptides were stored at -80°C until use. Then, they were dissolved in MilliQ H_2O with 10 mM NaOH, followed by sonication for 5 minutes in an ice bath, this to dissolve possible preformed aggregates. The stock solutions of monomeric Aβ peptide were diluted to the desired concentrations in either sodium phosphate buffer (for the AFM, CD and NMR experiments) or MES buffer (for the fluorescence experiments). All sample preparation steps were performed on ice. The concentration of the dissolved

peptide was initially estimated from the dry weight of the peptide powder and then more accurately spectroscopically quantified using a NanoDrop instrument (Eppendorf SE, Germany).

For the fluorescence spectroscopy measurements, the $A\beta_{40}$ peptide powder was first dissolved in HFIP to a concentration of 100 μM, to disassemble possible pre-formed peptide aggregates into monomers. The peptide solution was then divided into aliquots and the HFIP was evaporated under vacuum. The resulting tubes with $A\beta_{40}$ film were stored at -80°C. Before the fluorescence measurements, the $A\beta_{40}$ samples were dissolved in 0.02% NH_4OH to a stock concentration of 80 μM.

3.2 Circular dichroism spectroscopy of Aβ secondary structure

Circular Dichroism (CD) measurements were performed on a Chirascan CD spectrometer from Applied Photophysics, UK, operating at 20°C. Aβ peptide samples of 10 μM concentration, either $A\beta_{40}$ wt or NoHis, in 20 mM sodium phosphate buffer, pH 7.3, were measured in a quartz cuvette with 2 mm path length and 600 μl sample volume. The CD spectra were recorded between 190 and 260 nm, with a step size of 0.5 nm and 5 seconds sampling time.

After initial measurements in buffer only, 50 mM SDS detergent was added to each sample, followed by titrations with small amounts of $CoCl_2$. As the critical micelle concentration (cmc) for SDS is 8.2 mM in water at 25°C [84], 50 mM SDS is clearly enough to induce micelle formation. With on average 62 SDS molecules per micelle [85], 50 mM of SDS molecules roughly correspond to 0.8 mM of SDS micelles. This is almost 100x more than the $A\beta_{40}$ peptide concentration (10 μM), which means that no micelle should host more than a single $A\beta_{40}$ peptide. As these isolated $A\beta_{40}$ peptides will not aggregate, the measurements conducted in presence of SDS only record interactions between Co(II) ions and $A\beta_{40}$ monomers.

A binding curve for the Co(II)·$A\beta_{40}$ complex was produced by plotting the CD intensity at 208 nm versus the concentration of added Co(II) ions. Apparent dissociation constants for this Co(II)·$A\beta_{40}$ complex, K_D^{App}, were computed by fitting the data curve to the so-called Morrison equation [86]:

$$\mathrm{I} = \mathrm{I}_0 + \frac{\mathrm{I}_\infty - \mathrm{I}_0}{2 \cdot [\mathrm{A}\beta\,]} \cdot \left((\mathrm{K_D} + [\mathrm{Me}] + [\mathrm{A}\beta\,]) - \sqrt{(\mathrm{K_D} + [\mathrm{Me}] + [\mathrm{A}\beta\,])^2 - 4 \cdot [\mathrm{Me}] \cdot [\mathrm{A}\beta\,]} \right)$$

(Eq. 1)

In this equation, K_D is the apparent dissociation constant, [Me] is the concentration of added metal ions, [Aβ] is the concentration of the $A\beta_{40}$ peptide, I_0 is the initial fluorescence intensity before addition of metal ions, and I_∞ is the steady-state intensity at the end of the titration. This version of the equation assumes a single binding site for the metal ion. It did not appear necessary to add a linear term for the fluorescence quenching effect of free (unbound) metal ions [87]. Because no corrections were made for possible

interactions between the metal ions and the MES buffer, the calculated dissociation constants should be considered apparent (K_D^{App}).

3.3 Fluorescence spectroscopy of metal ion binding to $A\beta_{40}$

For the fluorescence quenching experiments, samples of $A\beta_{40}$ were diluted to 10 μM concentration in 20 mM MES buffer, pH = 7.3, and put in quartz cuvettes with 5 mm path length (600 μL sample volume). The fluorescence emission intensity at 305 nm (excitation wavelength 270 nm) was recorded at 25°C using a Perkin Elmer LS-55 fluorescence spectrophotometer (Waltham, MA, USA) equipped with a magnetic stirrer. The titrations were carried out by consecutive additions of 1 μL aliquots of 1.2–12 mM stock solutions of $Cu(OAc)_2$ dissolved in 20 mM MES buffer, pH = 7.3. After each addition of $Cu(OAc)_2$, the solution was stirred for 30 s before recording fluorescence emission spectra. To investigate possible $A\beta_{40}$ binding competition between Cu(II) and Co(II) ions, the Cu(II) titrations were carried out both with and without 50 μM $CoCl_2$ being present in the samples. The resulting Cu(II) binding curves, recorded in the absence or presence of Co(II) ions, were analyzed using the Origin v8.5 software (OriginLab Corp., USA). Apparent dissociation constants for the Cu(II)·$A\beta_{40}$ complex, K_D^{App}, were computed by fitting the Cu(II) binding curves to Eq. 1 (above).

3.4 NMR spectroscopy of the Co(II)·$A\beta_{40}$ complex

Nuclear magnetic resonance (NMR) spectroscopy was carried out using a Bruker Avance instrument (700 MHz) equipped with a cryoprobe. Two-dimensional ^{1}H,^{15}N-HSQC and ^{1}H,^{13}C-HSQC spectra were measured at 5°C using samples of 84 μM monomeric ^{15}N- and ^{15}N,^{13}C-labelled $A\beta_{40}$ peptide in 20 mM sodium phosphate buffer (90/10 H_2O/D_2O) at either pH 7.3 or pH 5.6. Then, $CoCl_2$ was titrated to the samples. One titration was performed in the presence of 50 mM of the SDS detergent, in order to mimic a membrane environment. The NMR data was processed with the Topspin v.3.6.2 software, and previously published data was used to assign the HSQC crosspeaks at both neutral pH [88–90] and acidic pH [91].

3.5 Thioflavin T kinetics of $A\beta_{40}$ aggregation

Samples containing 10 μM $A\beta_{40}$, 20 mM MES buffer (pH 7.3) and 20 μM ThT dye, together with increasing concentrations of $CoCl_2$ (0, 0.5, 2, 5, 20 and 200 μM), were incubated in a 96-well microplate with a well sample volume of 100 μl. ThT is a benzothiazole dye that increases its fluorescence intensity upon binding to amyloid material [92]. Three replicates of each condition were prepared, and a FLUOstar Omega microplate reader (BMG Labtech, Germany) was used to record the effect of Co(II) ions on $A\beta_{40}$ amyloid aggregation. The samples were monitored during incubation for 15 hrs at 37°C. The ThT emission intensity at 480 nm (excitation wavelength 440 nm) was measured every five minutes, and each five-minute cycle contained 140 seconds of shaking at 200 rpm. The measurement data was fitted to a modified sigmoid function in order to obtain parameters describing the aggregation process [92]:

$$F(t) = F_0 + m_1 \bullet t + \frac{F_{end} + m_2 \bullet t}{(1+\exp(\frac{T_{1/2}-t}{tau}))} \quad \text{(Eq. 2)}$$

Here, F(t) is the measured ThT fluorescence over time, F_0 and F_{end} are the initial and final ThT fluorescence intensities, respectively, m_1 and m_2 are the slopes of the initial and final

baselines, $T_{½}$ is the aggregation half-time, and *tau* is the elongation time constant [92].

3.6 AFM imaging of $Aβ_{40}$ aggregates

$Aβ_{40}$ peptide samples were diluted to 10 μM concentration in 10 mM sodium phosphate buffer, pH 7.3, together with either 0 μM, 1 μM, 10 μM or 50 μM $CoCl_2$, and then incubated at 37°C during 24 hrs. After incubation, 20 μL of each sample were deposited on freshly cleaved mica sheets for 30 minutes, and then washed several times with around 10 mL of deionized water before being dried overnight at room temperature. AFM imaging was performed on a BioScope Catalyst AFM unit (Bruker corp., USA), using Bruker SNL10 cantilevers operating in peak force tapping mode in air. The image resolution was set to 512 x 512 pixels, the scan rate was 0.51 Hz, the scan size was 15 x 15 μm, and the color scale was set at (-2 : 4 nm).

4. Results

4.1 CD spectroscopy measurements of Aβ secondary structure

CD spectroscopy was used to investigate possible effects of Co(II) ions on the secondary structures of $Aβ_{40}$ and $Aβ_{NoHis}$ peptides. In aqueous buffer, both peptides displayed CD spectra with minima around 198 nm (Figs. 1A and 1B, black spectra), which is typical for random coil structure [93]. The 198 nm intensity was around − 13.000 for $Aβ_{40}$ and − 11.000 for $Aβ_{NoHis}$, indicating a more pronounced random coil structure in the $Aβ_{40}$ peptide. After addition of 50 mM SDS detergent, which is known to form membrane-mimicking micelles [85], both peptides adopted CD spectra with characteristic minima at 208 and 222 nm (Figs. 1A and 1B, red spectra), which corresponds to α-helix structure [93]. It has previously been shown that when positioned in SDS micelles, the two Aβ segments 15–25 and 29–35 adopt α-helical structure [94]. The observed 208 nm intensities in the SDS environment were − 11.600 for $Aβ_{40}$ and − 11.700 for $Aβ_{NoHis}$ (Fig. 1; Table 1), suggesting a similar amount of α-helix in the two peptides.

Titrating Co(II) ions to the $Aβ_{40}$ sample had a distinct effect on the peptide´s secondary structure. The overall shape of the CD signal remained the same, but the CD intensity around the 208 nm minimum gradually decreased (Fig. 1A). The isodichroic point around 197 nm (Fig. 1A) showed that this Co(II)-induced structural change was a well-defined two-state transition. The changes in the CD spectra resulted in changes in the 222/208 nm intensity ratio (Table 1), which is known to correspond to changes in coil-coil interactions, i.e. when two or more α-helices form coiled coils (helix supercoiling) via hydrophobic interactions [17, 95–97]. In such structures, a 222/208 ratio close to 1 reflects large amounts of superhelicity [98]. For Aβ monomers in SDS, the coil-coil interactions most likely result from the two α-helical segments 15–25 and 29–35 interacting with each other [94]. As discussed in the Methods section,

the SDS micelles contain single monomeric $A\beta_{40}$ peptides, rendering coil-coil interactions between multiple $A\beta_{40}$ peptides unlikely. After addition of 512 μM Co(II), the CD signal at 208 nm decreased from − 11600 to -10000, while the 222 nm signal only decreased from − 7900 to -7600 (Fig. 1A; Table 1). Thus, the ratio of the 222/208 signal intensities gradually increased from 0.68 without Co(II) ions to 0.77 with 512 μM Co(II) added (Table 1).

For the $A\beta_{NoHis}$ mutant, addition of Co(II) ions produced a much weaker structural effect than in wt $A\beta_{40}$ (Fig. 1B). Without added Co(II), the CD intensities were − 11.700 at 208 nm and − 8.500 at 222 nm, yielding a 222/208 ratio of 0.73 (Table 1). With 512 μM Co(II) added, the 208 nm intensity was − 11.500, the 222 nm intensity was − 8.700, and the 222/208 ratio was 0.75. The resulting change in 222/208 ratio from 0.73 to 0.75 in $A\beta_{NoHis}$ is clearly much smaller than the Co(II)-induced change from 0.68 to 0.76 induced in $A\beta_{40}$ (Table 1). This indicates that the His residues, which are missing in the $A\beta_{NoHis}$ mutant, are involved in Co(II) binding. An alternative explanation, although less likely, is that the His residues present in wt $A\beta_{40}$ are required for the Co(II)-induced coil-coil interactions that underlie the observed structural change.

Table 1
CD intensities at 208 nm and 222 nm for 10 μM $A\beta_{40}$ and $A\beta_{NoHis}$ peptides in 50 mM SDS and 20 mM phosphate buffer, pH 7.3 at 20°C, at increasing concentrations of Co(II) ions.

	Wavelength (nm)	0μM Co(II)	2μM Co(II)	6μM Co(II)	16μM Co(II)	56μM Co(II)	156μM Co(II)	256μM Co(II)	512μM Co(II)
$A\beta_{40}$	208	-11598	-11755	-11645	-11653	-11242	-10723	-10450	-9973
	222	-7925	-8109	-7935	-8080	-7957	-7890	-7795	-7648
	222/208 ratio	0.68	0.69	0.68	0.69	0.71	0.74	0.75	0.77
Aβ NoHis	208	-11717	-11909	-12037	-12171	-12154	-11976	-12001	-11545
	222	-8495	-8772	-8797	-8867	-9018	-8924	-8912	-8668
	222/208 ratio	0.73	0.74	0.73	0.73	0.74	0.74	0.74	0.75

Given the large Co(II)-induced change in CD signal at 208 nm in $A\beta_{40}$ (Table 1), it was possible to produce a Co(II) binding curve by plotting the CD intensity at 208 nm *vs* Co(II) concentration (Fig. 2A). Fitting Eq. 1 to this binding curve yielded an apparent binding constant of 271 μM for the Co(II)·$A\beta_{40}$ complex (Fig. 2A). As the CD experiment was not designed to measure binding affinities, but rather to monitor changes in secondary structure, there is some uncertainty in the measured K_D value. Thus, we considered the K_D value to be an approximation around 0.3 mM.

4.2 Fluorescence spectroscopy measurements of Cu(II) and Co(II) binding to Aβ

Fluorescence spectroscopy was carried out to estimate the binding affinity of the Co(II)·$A\beta_{40}$ complex. For metal ions that quench fluorescence signals, such as Ag(I), Cu(II) and Hg(II), binding affinities of metal-protein complexes can be measured via the quenching effect on amino acids with intrinsic fluorescence, such as Tyr and Trp

[17, 87, 91, 99, 100]. However, initial experiments showed that Co(II) induced very small quenching of Tyr and Trp fluorescence (data not shown). It was therefore not possible to use fluorescence spectroscopy for direct measurements of the binding affinity of the Co(II)·$A\beta_{40}$ complex. Instead, this binding affinity was estimated from experiments of binding competition between Co(II) and Cu(II) ions to the $A\beta_{40}$ peptide

[101–103]. Cu(II) is known to bind to the N-terminal Aβ segment via the N-terminal His residues, and to strongly quench the fluorescence of Tyr10, the only native fluorophore in Aβ peptides [87, 104]. The current CD and NMR results (below) indicate that Co(II) ions coordinate to the $A\beta_{40}$ peptide via the N-terminal His residues, implying that Co(II) and Cu(II) ions should compete for the same binding site.

Figure 2B shows titrations of Cu(II) to $A\beta_{40}$, conducted both with and without 50 μM $CoCl_2$ being present in the sample. Three titrations were carried out for each condition. The apparent K_D^{App} values for the $A\beta_{40}$·Cu(II) complex, obtained from fitting Eq. 1 to the titration curves, are 1.6 μM, 1.5 μM and 1.7 μM without $CoCl_2$, i.e. on average 1.6 ± 0.1 μM (Table 2). These values are similar to those of earlier measurements of the $A\beta_{40}$·Cu(II) complex [91, 101]. With 50 μM $CoCl_2$ in the sample, the affinity values for Cu(II) binding were 0.8 μM, 1.1 μM and 1.6 μM, i.e. on average 1.2 ± 0.4 μM (Table 2). The small difference between the average K_D^{App} values recorded with and without $CoCl_2$ was found to be not statistically significant at the 5% level, using a two-tailed t-test.

Overall, these measurements show that Co(II) ions are unable to effectively compete with Cu(II) ions for binding to $A\beta_{40}$. Given that Cu(II) exhibits an apparent binding affinity of approximately 1 μM, the affinity of Co(II) for $A\beta_{40}$ must be at least one order of magnitude weaker. The fluorescence results shown in Fig. 2B are therefore fully consistent with the Co(II) affinity value of 0.3 mM derived from the CD measurements (Fig. 2A).

Table 2
Apparent binding affinities (K_D^{App}) in μM for Cu(II) binding to $A\beta_{40}$, recorded with and without 50 μM Co(II) ions in the sample.

Buffer only	**1**	**2**	**3**	**Mean**
	1.61 ± 0.97	**1.54 ± 0.44**	**1.74 ± 0.44**	**1.6 ± 0.1**
With 50 μM Co(II)	0.78 ± 0.20	1.10 ± 0.52	1.60 ± 0.58	1.2 ± 0.4

4.3 NMR spectroscopy measurements of the Aβ·Co(II) complex

High-resolution NMR experiments were carried out to investigate possible residue-specific molecular interactions between monomeric $A\beta_{40}$ peptide and Co(II) ions. Figure 3 shows 2D $^{1}H,^{15}N$-HSQC spectra for the amide cross-peak region of 92 μM $^{13}C,^{15}N$-labeled $A\beta_{40}$ peptides, at either pH 7.3 or pH 5.6, recorded before and after addition of Co(II) ions in Co(II):$A\beta_{40}$ ratios of 1:2, 1:1 and 10:1.

For $A\beta_{40}$ in buffer at pH 7.3, adding Co(II) ions induces a concentration-dependent loss of amide cross-peak intensity, especially for N-terminal $A\beta_{40}$ residues (Fig. 3A). This indicates residue-specific Co(II) binding in this region. The N-terminal cross-peak intensity loss is likely caused by intermediate (on the NMR time-scale) chemical exchange between a free state and a Co(II)-bound state of the $A\beta_{40}$ peptide, similar to the effect caused by binding of Zn(II) ions (Danielsson et al., 2007). As the Co(II) ion has a paramagnetic $[Ar]3d^7$ electron configuration with unpaired d-electrons, there should also be a paramagnetic quenching effect of the NMR signals at the binding site [105]. Furthermore, a general loss of cross-peak intensity affecting all $A\beta_{40}$ residues can be observed, especially at high $CoCl_2$ concentrations (Fig. 3A). This effect might be caused by non-specific Co(II) binding, or more likely by Co(II) promoting formation of Aβ aggregates that either precipitate out of the solution or are too large and/or heterogeneous to be observed with HSQC NMR [106]. Thus, the HSQC spectra in Fig. 3 only report on interactions between Co(II) ions and non-aggregated $A\beta_{40}$ monomers.

In aqueous buffer at pH 5.6, the reduction in cross-peak intensity after added Co(II) ions is weaker than at neutral pH, and there is no distinct specific loss of intensity in the N-terminal region (Fig. 3C). This indicates that Co(II) binding to $A\beta_{40}$ is both weaker and less residue-specific at acidic pH. The main difference between pH 7.3 and pH 5.6 is that His residues become protonated at the lower pH, as they have pKa values around 6.8 in short peptides (Pogostin et al., 2019). Naturally, protonated His residues are less prone to bind cationic metal ions. The weaker and less residue-specific Co(II) binding at pH 5.6 therefore suggests that Co(II) ions bind to $A\beta_{40}$ via the N-terminal His residues His6, His13 and His14.

Co(II)-induced loss of cross-peak intensity for N-terminal $A\beta_{40}$ residues is observed also for $A\beta_{40}$ peptides positioned in SDS micelles (Fig. 3B), which are a simple model for bio-membranes [85, 107]. The central and C-terminal Aβ regions are known to insert themselves as α-helices into SDS micelles [94, 107]. Thus, the $^{1}H,^{15}N$-HSQC spectrum for $A\beta_{40}$ in SDS micelles mainly corresponds to an α-helical Aβ conformation (Fig. 3B). The N-terminal Aβ segment remains unstructured outside the SDS micelle surface [94], where it is available for interactions with e.g. metal ions [104]. The residue-specific loss of N-terminal cross-peak intensity visible in Fig. 3B shows that Co(II) ions bind the N-terminal part of $A\beta_{40}$ also when the monomeric peptide is positioned in a membrane-mimicking environment, with the N-terminal segment exposed to the solvent [94].

4.4 ThT fluorescence measurements of Aβ aggregation kinetics

To investigate the effect of Co(II) ions on $A\beta_{40}$ aggregation kinetics, samples containing 10 μM $A\beta_{40}$ were allowed to aggregate together with Thioflavin-T (ThT) dye and different amounts of Co(II) ions. The

resulting ThT curves are shown in Fig. 4, while the F_{end} and $T_{1/2}$ parameters obtained from fitting the curves to Eq. 2 are shown in Table 3. The two curves with highest Co(II) content do not display sigmoid shapes. Thus, although their initial and final fluorescence intensities are well-defined, meaningful time constants could not be derived from these curves (Table 3).

Two clear concentration-dependent effects were observed from the ThT measurements. First, the final ThT fluorescence intensities (F_{end}) of the $A\beta_{40}$ aggregation curves decrease with increasing amounts of Co(II) ions (Fig. 4; Table 3). In principle, this might be explained by Co(II) ions quenching the ThT fluorescence signal. But separate experiments showed that Co(II) ions do not have such quenching effects, as is further discussed below (the measurements of Aβ intrinsic fluorescence). Instead, the reduction in ThT fluorescence intensity is caused by Co(II) inhibiting formation of amyloid fibrils, thereby giving the ThT molecules less amyloid material to bind to. This explanation is compatible with the AFM results (below), which also show that Co(II) interferes with Aβ fibrillation (Fig. 5).

The second trend, which is clear from the first four curves in Fig. 4, is that Co(II) ions increase the Aβ aggregation half-time (Table 3). This second trend arguably has the same explanation as the first: if Co(II) interferes with Aβ fibrillation, then it should take longer time for the fibrils to form.

Table 3
Aggregation half-times ($T_{1/2}$) and final ThT fluorescence intensities (F_{end}) for $A\beta_{40}$ fibril formation with different concentrations of Co(II) ions, obtained by fitting the curves in Fig. 4 to Eq. 2.

Co (II)	0 μM	0.5 μM	2 μM	5 μM	20 μM	200 μM
F_{end}	2767	1788	1235	1192	1096	707
$T_{1/2}$ (hrs)	1.8	1.6	2.5	3.5	n/a	n/a

4.5 AFM images of Aβ peptide aggregates

To investigate the influence of Co(II) ions on $A\beta_{40}$ fibril formation, we recorded AFM images (Fig. 5) of $A\beta_{40}$ aggregates formed after 24 hrs of incubation together with different amounts of Co(II). With no added $CoCl_2$, 10 μM $A\beta_{40}$ formed typical long (5–20 μm) and slender amyloid fibrils with an apparent height (diameter) around 4–5 nm (Fig. 5A). This is consistent with previously published images of Aβ fibrils formed *in vitro* [16, 108–112].

Similar numerous long and slender fibrils were observed also in the presence of 1 μM Co(II) ions (Fig. 5B). However, after addition of 10 μM Co(II) ions, i.e. a 1:1 Co(II):$A\beta_{40}$ ratio, most observed fibrils were very short, in the range of 2–4 μm (Fig. 5C) These short fibrils have a similar height as the long ones, i.e. 4–5 nm. Some occasional long fibrils were also present in the sample. With 50 μM Co(II) ions added the long fibrils were completely gone, as only a large number of the 2–4 μm short fibrils could be observed (Fig. 5D). These images show that Co(II) has a clear concentration-dependent effect on the $A\beta_{40}$ fibrillation process, mainly by interfering with fibril elongation.

5. Discussion

Co is known to be neurotoxic, but its possible role in neurodegenerative diseases remains unclear [24, 113]. Numerous studies have investigated how transition metals such as Cu and Zn and heavy metals such as Hg and Pb might be involved in AD etiology and/or pathogenesis, with an emphasis on metal ion interactions with Aβ peptides [14–17]. Here, we interpret our results on Aβ interactions with Co(II) ions in the light of this earlier work.

5.1 Residue-specific binding of Co(II) to $Aβ_{40}$ monomers

Our CD spectroscopy results show that Co(II) binding to single $Aβ_{40}$ peptides positioned in SDS micelles, a simple membrane-mimicking system [85], induce changes in the $Aβ_{40}$ secondary structure (Fig. 1A). Specifically, adding Co(II) increases the amount of intramolecular coil-coil interactions. While $Aβ_{40}$ monomers typically adopt random coil conformations in aqueous buffer [12], they prefer α-helical structures in membrane environments [14, 94, 114], where α-helical conformations may promote peptide aggregation [14, 115].

The CD measurements indicate that Co(II) displays relatively weak binding to $Aβ_{40}$, i.e. around 0.3 mM (Fig. 2A). This result is compatible with the fluorescence quenching measurements, which show that Co(II) ions are not able to effectively compete with Cu(II) ions for binding to $Aβ_{40}$ (Fig. 2B). The apparent affinity value of 0.3 mM is also generally compatible with an earlier study of Aβ binding to metal ions, which however did not report actual K_D values [35].

According to the Irving-Williams series [116], the binding affinities to peptides and proteins should follow the order Mn(II) < Fe(II) < Co(II) < Ni(II) < Cu(II) > Zn(II). We have previously reported apparent K_D values around 50–100 μM for Mn(II) in phosphate buffer, pH 7.35 [117], around 1–10 μM for Zn(II) in phosphate or Hepes buffer, pH 7.2 [102], around 0.5–2.5 μM for Cu(II) in phosphate or Hepes buffer, pH 7.2 – pH 7.35 [87, 102, 104], and around 5–10 μM for Ni(II) in 20 mM phosphate buffer, pH 7.3 [118]. Thus, our current measurements suggest that Co(II) displays weaker binding to $Aβ_{40}$ than all of Cu(II), Mn(II), Ni(II), and Zn(II), which is not in line with the Irving-Williams series. However, it is well known that binding affinity measurements are influenced by factors such as pH, buffer, temperature and the experimental technique [91, 119]. It is not immediately clear that K_D values derived from CD data can be directly compared to K_D values derived from fluorescence or NMR spectroscopy, and future studies might be able to investigate Aβ binding to Co(II) and Mn(II) ions in more detail.

The current CD results furthermore indicate that Aβ His residues are involved in coordinating Co(II) ions, as they induce virtually no structural changes in the $Aβ_{NoHis}$ mutant (Fig. 1B). Earlier studies have reported that Co(II) binds to His residues in Aβ fragments [34, 35], and it is generally known that Co(II) preferably binds to histidine (His), cysteine (Cys), aspartic acid (Asp) and glutamic acid (Glu) residues, in that order [120–123]. Specifically, most interactions between Co(II) and proteins occur via the two nitrogen atoms in the His side chain [72].

Our NMR results show that at neutral pH, both in aqueous buffer and in SDS micelles, equimolar amounts of Co(II) display residue-specific binding to the N-terminal segment of the $A\beta_{40}$ peptide (Figs. 3A and 3B). The absence of such residue-specific Co(II) binding at low pH (Fig. 3C) supports His6, His13, and His14 being involved in Co(II) binding, as these residues become protonated at acidic pH and thereby less prone to interact with cations [87, 91]. Thus, together with e.g. Ag(I), Cu(II), Fe(II), Hg(II), Mn(II), Ni(II), Zn(II), and possibly Pb(IV), Co(II) appears to belong to a family of metal ions that bind the Aβ N-terminal segment mainly via His residues [12, 16, 17, 35, 91, 100, 103, 117, 124–126]. Yet, the exact binding coordination for Co(II) could not be determined from our measurements, and it is possible that multiple alternating binding conformations exists, as has been shown for e.g. Cu(II) ions [15]. Because the difference between the $A\beta_{40}$ and the $A\beta_{42}$ peptides is the additional C-terminal Ile41 and Ala42 residues, and because Co(II) binds to the N-terminal segment, it is very likely that Co(II) binding is virtually identical for $A\beta_{40}$ and the longer and more toxic $A\beta_{42}$.

Our AFM and ThT fluorescence experiments show that Co(II) interferes with $A\beta_{40}$ fibrillation in a concentration-dependent manner (Figs. 4 and 5). This is consistent with earlier studies showing that cobalt complexes can modulate Aβ aggregation [30–33].

The AFM images suggest that Co(II) impedes fibril elongation (Fig. 5). Such effects have previously been observed and described in detail for Zn(II) and Ag(I) ions [126, 127]. As Co(II) binds to the same N-terminal Aβ metal binding site as Zn(II) and Ag(I), with His6, His13, and His14 as main binding residues, it is likely that all three metal ions impede Aβ fibril elongation with the same mechanism. The clear effect on Aβ fibril formation induced by equimolar amounts of Co(II) shown in Fig. 4C might appear surprising, given the somewhat weak affinity (i.e., 0.3 mM) of Co(II) for Aβ monomers (Fig. 2A). However, a previous study showed that Ca(II) ions had a strong positive effect on Aβ fibrillation, even though Ca(II) displayed weak binding to Aβ monomers [128]. The authors concluded that “the fibrillar architecture [is required] for binding” [128] page 195). A similar situation, with stronger affinity for Aβ aggregates than Aβ monomers, might exist also for Co(II) ions. That would furthermore explain why elevated Co concentrations have been found in the amyloid plaques of AD brains [19], as these plaques mainly consist of Aβ aggregates [3]. The redox-active metal ions bound to these plaques, such as Cu(II), Co(II) and Fe(II), likely contribute to the oxidative stress observed in and around these plaques [28, 129–132].

The ThT fluorescence experiments show that Co(II) slows down $A\beta_{40}$ fibrillation and reduces the final amount of amyloid material in the samples (Fig. 4). Similar effects on Aβ aggregation have been observed for other heavy metal ions, such as Ag(I), Cd(III), Hg(I)/Hg(II), Ni(II), Pb(II), and uranyl [16, 17, 100, 103, 118, 126, 133]. It appears that many of these ions interfere with Abeta fibrillation by directing the aggregation pathways towards non-fibrillar amorphous aggregates. Co(II) might have a similar effect, especially as this ion previously has been shown to induce non-amyloid aggregation of proteins such as serum albumins [134, 135]. In fact, inducing misfolding and aggregation of proteins and peptides might be one of the molecular mechanisms of Co toxicity, and possibly of heavy metal toxicity in general [136, 137].

In summary, we here show that Co(II) ions bind to $A\beta_{40}$ peptides and modulate their aggregation. In addition to such modulation, Co(II) ions may also contribute to AD pathology by creating oxidative stress when bound to amyloid plaques, and by increasing Aβ production and the toxicity of Aβ oligomers [19, 28, 138, 139]. Although not a major risk factor for the general population, Co exposure might be related to AD pathogenesis in certain groups, such as people with orthopedic implants made from Co alloys [19, 113, 138].

6. Conclusions

We here show for the first time that Co(II) ions bind to the N-terminal segment of biologically relevant full-length $A\beta_{40}$ peptides, with the three N-terminal His6, His13, and His14 residues involved in binding coordination. The Co(II) binding affinity to Aβ is estimated to around 0.3 mM. Equimolar amounts of Co(II) inhibit normal Aβ fibrillation, mainly by interfering with fibril elongation, and induce structural alterations (coil-coil interactions) in Aβ monomers positioned in membrane-mimicking SDS micelles. Such effects on the structure and aggregation of peptides and proteins might be a general toxic mechanisms of Co(II).

References

1. Alzheimer´s_association (2025) Alzheimer's disease facts and figures. *Alzheimers Dement.* 21, e70235 (2025)
2. Scheltens P et al (2021) Alzheimer's disease. Lancet 397:1577–1590
3. Glenner GG, Wong CW (1984) Alzheimer's disease: initial report of the purification and characterization of a novel cerebrovascular amyloid protein. Biochem Biophys Res Commun 120:885–890
4. Sunde M, Blake CC (1998) From the globular to the fibrous state: protein structure and structural conversion in amyloid formation. Q Rev Biophys 31:1–39
5. Miller LM et al (2006) Synchrotron-based infrared and X-ray imaging shows focalized accumulation of Cu and Zn co-localized with beta-amyloid deposits in Alzheimer's disease. J Struct Biol 155:30–37
6. Lee SJC, Nam E, Lee HJ, Savelieff MG, Lim MH (2017) Towards an understanding of amyloid-β oligomers: characterization, toxicity mechanisms, and inhibitors. Chem Soc Rev 46:310–323
7. Selkoe DJ, Hardy J (2016) The amyloid hypothesis of Alzheimer's disease at 25 years. EMBO Mol Med 8:595–608
8. Luo J, Wärmländer SKTS, Gräslund A, Abrahams JP (2016) Cross-interactions between the Alzheimer Disease Amyloid-β Peptide and Other Amyloid Proteins: A Further Aspect of the Amyloid Cascade Hypothesis. J Biol Chem 291:16485–16493
9. Glabe CG (2008) Structural classification of toxic amyloid oligomers. J Biol Chem 283:29639–29643
10. Ghosh S, Ali R, Verma S (2023) Aβ-oligomers: A potential therapeutic target for Alzheimer's disease. Int J Biol Macromol 239:124231

11. Owen MC et al (2019) Effects of in vivo conditions on amyloid aggregation. Chem Soc Rev 48:3946–3996
12. Wärmländer S et al (2013) Biophysical studies of the amyloid β-peptide: interactions with metal ions and small molecules. Chembiochem Eur J Chem Biol 14:1692–1704
13. Abelein A et al (2014) The hairpin conformation of the amyloid β peptide is an important structural motif along the aggregation pathway. J Biol Inorg Chem JBIC Publ Soc Biol Inorg Chem 19:623–634
14. Wärmländer SKTS et al (2019) Metal binding to the amyloid-β peptides in the presence of biomembranes: potential mechanisms of cell toxicity. J Biol Inorg Chem JBIC Publ Soc Biol Inorg Chem 24:1189–1196
15. Faller P (2009) Copper and Zinc Binding to Amyloid-β: Coordination, Dynamics, Aggregation, Reactivity and Metal-Ion Transfer. *ChemBioChem* 10, 2837–2845
16. Wallin C et al (2017) Alzheimer's disease and cigarette smoke components: effects of nicotine, PAHs, and Cd(II), Cr(III), Pb(II), Pb(IV) ions on amyloid-beta peptide aggregation. *Sci Rep* 7, 14423
17. Berntsson E et al (2025) Binding of Hg(I) and Hg(II) Ions to Amyloid-Beta (Abeta) Peptide Variants Affect their Structure and Aggregation. *Chembiochem* e2500252 10.1002/cbic.202500252
18. Bourassa MW et al (2013) Elevated copper in the amyloid plaques and iron in the cortex are observed in mouse models of Alzheimer's disease that exhibit neurodegeneration. Biomed Spectrosc Imaging 2:129–139
19. Ebner BA et al (2025) Brain tissue metal concentrations and Alzheimer's disease neuropathology in total joint arthroplasty patients versus controls. Acta Neuropathol (Berl) 149:18
20. Wang L et al (2020) Current understanding of metal ions in the pathogenesis of Alzheimer's disease. Transl Neurodegener 9:10
21. Das N, Raymick J, Sarkar S (2021) Role of metals in Alzheimer's disease. Metab Brain Dis 36:1627–1639
22. Singh SK et al (2022) Copper-mediated β-amyloid toxicity and its chelation therapy in Alzheimer's disease. Metallomics 14:mfac018
23. Mezzanotte M, Stanga S (2024) Brain Iron Dyshomeostasis and Ferroptosis in Alzheimer's Disease Pathophysiology: Two Faces of the Same Coin. Aging Dis 16:2615–2640
24. Obied B et al (2024) Structure-Function Correlation in Cobalt-Induced Brain Toxicity. Cells 13:1765
25. Bocca B, Alimonti A, Bomboi G, Giubilei F, Forte G (2006) Alterations in the level of trace metals in Alzheimer's disease. Trace Elem Electrolytes 23:270–276
26. Gonzalez-Dominguez R, Garcia-Barrera T, Gomez-Ariza JL (2014) Characterization of metal profiles in serum during the progression of Alzheimer's disease. Metallomics 6:292–300
27. Zheng F et al (2019) Comparison of the neurotoxicity associated with cobalt nanoparticles and cobalt chloride in Wistar rats. Toxicol Appl Pharmacol 369:90–99
28. Chen J et al (2023) Cobalt nanoparticles induce mitochondrial damage and beta-amyloid toxicity via the generation of reactive oxygen species. Neurotoxicology 95:155–163

29. Zheng F et al (2021) Cobalt induces neurodegenerative damages through Pin1 inactivation in mice and human neuroglioma cells. J Hazard Mater 419:126378
30. Chan TG et al (2021) Modulation of amyloid-beta aggregation by metal complexes with a dual binding mode and their delivery across the blood-brain barrier using focused ultrasound. Chem Sci 12:9485–9493
31. Heffern MC et al (2014) Modulation of amyloid-beta aggregation by histidine-coordinating Cobalt(III) Schiff base complexes. ChemBioChem 15:1584–1589
32. Iscen A et al (2019) Inhibition of Amyloid-beta Aggregation by Cobalt(III) Schiff Base Complexes: A Computational and Experimental Approach. J Am Chem Soc 141:16685–16695
33. Yoo J et al (2025) Cobalt complexes as modulators against amyloid-beta aggregation. J Inorg Biochem 271:112972
34. Abdrakhmanov R, Blokhin DS, Usachev K, Klochkov V (2018) Modeling the Co2 + Binding to Amyloid Peptide Aβ13–23 in Water Environment by NMR Spectroscopy. BioNanoSci 8:423–427
35. Lermyte F et al (2019) Metal Ion Binding to the Amyloid beta Monomer Studied by Native Top-Down FTICR Mass Spectrometry. J Am Soc Mass Spectrom 30:2123–2134
36. Kobayashi M, Shimizu S (1999) Cobalt proteins. Eur J Biochem 261:1–9
37. Al-Amin ASM, Gupta V (2023) Vitamin B12 (Cobalamin). inStatPearls Publishing
38. Ankar A, Kumar A (2023) Vitamin B12 Deficiency. in *StatPearls*. Treasure Island (FL)
39. Apostoli P et al (2013) High doses of cobalt induce optic and auditory neuropathy. Exp Toxicol Pathol 65:719–727
40. Ikeda T et al (2010) Polyneuropathy caused by cobalt-chromium metallosis after total hip replacement. Muscle Nerve 42:140–143
41. Chen RJ, Lee VR (2024) Cobalt Toxicity. StatPearls. Treasure Island (FL)
42. Czarnek K, Terpilowska S, Siwicki AK (2015) Selected aspects of the action of cobalt ions in the human body. Cent Eur J Immunol 40:236–242
43. Holstein H, Ranebo Y, Raaf CL (2015) Human metabolism of orally administered radioactive cobalt chloride. J Env Radioact 143:152–158
44. Kettelarij J, Midander K, Liden C, Bottai M, Julander A (2018) Neglected exposure route: cobalt on skin and its associations with urinary cobalt levels. Occup Env Med 75:837–842
45. Princivalle A et al (2017) Biological monitoring of cobalt in hard metal factory workers. Int Arch Occup Env Health 90:243–254
46. Harrison-Brown M et al (2020) Limited penetration of cobalt and chromium ions into the cerebrospinal fluid following metal on metal arthroplasty: a cross-sectional analysis. Clin Toxicol Phila 58:233–240
47. Gomez-Arnaiz S, Tate RJ, Grant MH (2022) Cobalt Neurotoxicity: Transcriptional Effect of Elevated Cobalt Blood Levels in the Rodent Brain. *Toxics* 10
48. Fu X et al (2020) Perspectives on Cobalt Supply through 2030 in the Face of Changing Demand. Env Sci Technol 54:2985–2993

49. Godoy Leon MF, Dewulf J (2020) Data quality assessment framework for critical raw materials. The case of cobalt. Resour Conserv Recycl 157:104564
50. Tamihardja J et al (2022) Comparing Iridium-192 with Cobalt-60 sources in high-dose-rate brachytherapy boost for localized prostate cancer. Acta Oncol 61:714–719
51. Keegan GM, Learmonth ID, Case CP (2008) A systematic comparison of the actual, potential, and theoretical health effects of cobalt and chromium exposures from industry and surgical implants. Crit Rev Toxicol 38:645–674
52. Simonsen LO, Harbak H, Bennekou P (2012) Cobalt metabolism and toxicology–a brief update. Sci Total Env 432:210–215
53. Xia Z et al (2011) Characterization of metal-wear nanoparticles in pseudotumor following metal-on-metal hip resurfacing. Nanomed 7:674–681
54. Biglia A et al (2020) Cobalt hip prosthesis intoxication mimicking an autoimmune disease. Joint Bone Spine 87:652–654
55. Dahms K, Sharkova Y, Heitland P, Pankuweit S, Schaefer JR (2014) Cobalt intoxication diagnosed with the help of Dr House. Lancet 383:574
56. Dominguez-Garcia A et al (2023) Cobalt poisoning secondary to hip prosthesis: A case report. Farm Hosp 47:139–140
57. Mao X, Wong AA, Crawford R (2011) W. Cobalt toxicity–an emerging clinical problem in patients with metal-on-metal hip prostheses? Med J Aust 194:649–651
58. Peters RM, Willemse P, Rijk PC, Hoogendoorn M, Zijlstra WP (2017) Fatal Cobalt Toxicity after a Non-Metal-on-Metal Total Hip Arthroplasty. *Case Rep Orthop* 9123684 (2017)
59. Tower SS, Medlin DJ, Bridges RL, Cho CS (2020) Corrosion of Polished Cobalt-Chrome Stems Presenting as Cobalt Encephalopathy. Arthroplast Today 6:1022–1027
60. He C, Gao M, He T, Xing F (2025) Association of cobalt exposure with all-cause and cardiovascular mortality in U.S. adults. BMC Public Health 25:1757
61. Nordberg GF, Fowler BA, Nordberg M (2014) Handbook on the Toxicology of Metals. Elsevier Science & Technology, London, NETHERLANDS, THE
62. IARC. *Cobalt, Antimony Compounds, and Weapons-Grade Tungsten Alloy. IARC Monographs on the Identification of Carcinogenic Hazards to Humans, Volume 131*. (IARC, Lyon (FR), (2023)
63. Arslan S, Aksan S, Ucar R, Caliskaner AZ (2015) Contact dermatitis to cobalt chloride with an unusual mechanism. Prosthet Orthot Int 39:419–421
64. Sauni R et al (2010) Cobalt asthma–a case series from a cobalt plant. Occup Med Lond 60:301–306
65. Gregorowicz W, Pajchel L (2025) The Role of Cobalt Ions in Angiogenesis-A Review. Int J Mol Sci 26
66. Xu S et al (2025) Association between blood cobalt ion concentrations and anemia and cardiovascular diseases: novel evidence of toxicity resulting from metal implants. Front Nutr 12:1614771
67. Barceloux DG, Cobalt (1999) J Toxicol Clin Toxicol 37:201–206

68. Wang X, Yokoi I, Liu J, Mori A (1993) Cobalt(II) and nickel(II) ions as promoters of free radicals in vivo: detected directly using electron spin resonance spectrometry in circulating blood in rats. Arch Biochem Biophys 306:402–406
69. Angele-Martinez C et al (2023) Cobalt-mediated oxidative DNA damage and its prevention by polyphenol antioxidants. J Inorg Biochem 238:112024
70. Mohamed HRH et al (2025) Cobalt oxide nanoparticles induce cytotoxicity and excessive ROS mediated mitochondrial dysfunction and p53-independent apoptosis in melanoma cells. Sci Rep 15:2220
71. Baronas D et al (2024) Inhibitor binding to metal-substituted metalloenzyme: Sulfonamide affinity for carbonic anhydrase IX. J Inorg Biochem 256:112547
72. Khrustalev VV et al (2019) Cobalt(ii) cation binding by proteins. Metallomics 11:1743–1752
73. Nielsen JL et al (1997) Laser ablation inductively coupled plasma-mass spectrometry in combination with gel electrophoresis: a new strategy for speciation of metal binding serum proteins. Spectrochim Acta 53:339–345
74. Smith TA (2005) Human serum transferrin cobalt complex: stability and cellular uptake of cobalt. Bioorg Med Chem 13:4576–4579
75. Li J et al (2021) NOX2 activation contributes to cobalt nanoparticles-induced inflammatory responses and Tau phosphorylation in mice and microglia. Ecotoxicol Env Saf 225:112725
76. Olivieri G et al (2001) Melatonin protects SHSY5Y neuroblastoma cells from cobalt-induced oxidative stress, neurotoxicity and increased beta-amyloid secretion. J Pineal Res 31:320–325
77. Tower SS (2010) Arthroprosthetic cobaltism: neurological and cardiac manifestations in two patients with metal-on-metal arthroplasty: a case report. J Bone Jt Surg Am 92:2847–2851
78. Roos PM, Vesterberg O, Syversen T, Flaten TP, Nordberg M (2013) Metal concentrations in cerebrospinal fluid and blood plasma from patients with amyotrophic lateral sclerosis. Biol Trace Elem Res 151:159–170
79. Tandon L, Kasarskis E, Ehmann W (1995) Elemental imbalance studies by INAA on extraneural tissues from amyotrophic lateral sclerosis patients. J Radioanal Nucl Chem 195:13–19
80. White AR, Aschner M, Costa LG, Bush AI (2017) Biometals in Neurodegenerative Diseases : Mechanisms and Therapeutics. Elsevier Science & Technology, San Diego, UNITED STATES
81. Tang J et al (2023) Cobalt induces neurodegenerative damages through impairing autophagic flux by activating hypoxia-inducible factor-1α triggered ROS overproduction. Sci Total Environ 857:159432
82. Beba A et al (2023) Correlation of Blood Metal Concentrations with Cognitive Scores and Neuroimaging Findings in Patients with Total Joint Arthroplasty. J Alzheimers Dis 94:1335–1342
83. Jacobs JJ et al (2023) Could Alzheimer's Disease Pathology Be Associated With Metals Released From Total Hip Arthroplasty. *Orthop. Proc.* 105-B(SUPP_12), 32–32
84. Domínguez A, Fernández A, González N, Iglesias E, Montenegro L (1997) Determination of Critical Micelle Concentration of Some Surfactants by Three Techniques. J Chem Educ 74:1227–1231

85. Österlund N, Luo J, Wärmländer SKTS, Gräslund A (2019) Membrane-mimetic systems for biophysical studies of the amyloid-beta peptide. Biochim Biophys Acta Proteins Proteom 1867:492–501
86. Kuzmic P (2015) History, variants and usage of the 'Morrison equation' in enzyme inhibition kinetics, BioKin Technical Note TN-2015-01 [Online]
87. Lindgren J et al (2013) Engineered non-fluorescent Affibody molecules facilitate studies of the amyloid-beta (Abeta) peptide in monomeric form: low pH was found to reduce Abeta/Cu(II) binding affinity. J Inorg Biochem 120:18–23
88. Danielsson J, Andersson A, Jarvet J, Gräslund (2006) A. 15N relaxation study of the amyloid beta-peptide: structural propensities and persistence length. Magn Reson Chem 44:21 Spec No, S114-
89. Roche J, Shen Y, Lee JH, Ying J, Bax A, Monomeric (2016) Abeta(1–40) and Abeta(1–42) Peptides in Solution Adopt Very Similar Ramachandran Map Distributions That Closely Resemble Random Coil. Biochemistry 55:762–775
90. Yamaguchi T, Matsuzaki K, Hoshino M (2011) Transient formation of intermediate conformational states of amyloid-beta peptide revealed by heteronuclear magnetic resonance spectroscopy. FEBS Lett 585:1097–1102
91. Ghalebani L, Wahlström A, Danielsson J, Wärmländer SK, Gräslund A (2012) pH-dependence of the specific binding of Cu(II) and Zn(II) ions to the amyloid-beta peptide. Biochem Biophys Res Commun 421:554–560
92. Gade Malmos K et al (2017) ThT 101: a primer on the use of thioflavin T to investigate amyloid formation. Amyloid 24:1–16
93. Wärmländer SKTS, Lakela AL, Berntsson E, Jarvet J, Gräslund A (2025) Secondary Structures of Human Calcitonin at Different Temperatures and in Different Membrane-Mimicking Environments, Characterized by Circular Dichroism (CD) Spectroscopy. ACS Omega 10:17133–17142
94. Jarvet J, Danielsson J, Damberg P, Oleszczuk M, Gräslund A (2007) Positioning of the Alzheimer Abeta(1–40) peptide in SDS micelles using NMR and paramagnetic probes. J Biomol NMR 39:63–72
95. Lau SY, Taneja AK, Hodges RS (1984) Synthesis of a model protein of defined secondary and quaternary structure. Effect of chain length on the stabilization and formation of two-stranded alpha-helical coiled-coils. J Biol Chem 259:13253–13261
96. Zhou NE, Kay CM, Hodges RS (1992) Synthetic model proteins: the relative contribution of leucine residues at the nonequivalent positions of the 3–4 hydrophobic repeat to the stability of the two-stranded alpha-helical coiled-coil. Biochemistry 31:5739–5746
97. Zhou NE, Kay CM, Hodges RS (1992) Synthetic model proteins. Positional effects of interchain hydrophobic interactions on stability of two-stranded alpha-helical coiled-coils. J Biol Chem 267:2664–2670
98. Barbar E, Nyarko ANMR (2014) Characterization of Self-Association Domains Promoted by Interactions with LC8 Hub Protein. Comput Struct Biotechnol J 9:e201402003
99. Berntsson E et al (2022) Mercury Ion Binding to Apolipoprotein E Variants ApoE2, ApoE3, and ApoE4: Similar Binding Affinities but Different Structure Induction Effects. ACS Omega 7:28924–28931

100. Lakela AL et al (2025) Molecular interactions, structural effects, and binding affinities between silver ions (Ag(+)) and amyloid beta (Abeta) peptides. Sci Rep 15:5439
101. Berntsson E et al (2021) Lithium ions display weak interaction with amyloid-beta (Abeta) peptides and have minor effects on their aggregation. Acta Biochim Pol 68:169–179
102. Danielsson J, Pierattelli R, Banci L, Gräslund A (2007) High-resolution NMR studies of the zinc-binding site of the Alzheimer's amyloid beta-peptide. FEBS J 274:46–59
103. Wallin C et al (2020) Mercury and Alzheimer's Disease: Hg(II) Ions Display Specific Binding to the Amyloid-beta Peptide and Hinder Its Fibrillization. Biomolecules 10:44
104. Tiiman A et al (2016) Specific Binding of Cu(II) Ions to Amyloid-Beta Peptides Bound to Aggregation-Inhibiting Molecules or SDS Micelles Creates Complexes that Generate Radical Oxygen Species. J Alzheimers Dis 54:971–982
105. Barnhart JL, Berk RN (1986) Influence of paramagnetic ions and pH on proton NMR relaxation of biologic fluids. Invest Radiol 21:132–136
106. Fawzi NL, Ying J, Torchia DA, Clore GM (2010) Kinetics of amyloid beta monomer-to-oligomer exchange by NMR relaxation. J Am Chem Soc 132:9948–9951
107. Österlund N et al (2018) Amyloid-beta Peptide Interactions with Amphiphilic Surfactants: Electrostatic and Hydrophobic Effects. ACS Chem Neurosci 9:1680–1692
108. Luo J et al (2013) Inhibiting and reversing amyloid-beta peptide (1–40) fibril formation with gramicidin S and engineered analogues. Chemistry 19:17338–17348
109. Luo J, Wärmländer SK, Gräslund A, Abrahams JP (2013) Human lysozyme inhibits the in vitro aggregation of Abeta peptides, which in vivo are associated with Alzheimer's disease. Chem Commun Camb 49:6507–6509
110. Luo J, Wärmländer SK, Gräslund A, Abrahams JP (2016) Reciprocal Molecular Interactions between the Abeta Peptide Linked to Alzheimer's Disease and Insulin Linked to Diabetes Mellitus Type II. ACS Chem Neurosci 7:269–274
111. Król S et al (2021) The amyloid-inhibiting NCAM-PrP peptide targets Aβ peptide aggregation in membrane-mimetic environments. iScience 24:102852
112. Paul S et al (2023) 13C- and 15N-labeling of amyloid-β and inhibitory peptides to study their interaction via nanoscale infrared spectroscopy. Commun Chem 6:163
113. Wu T, Li H, Chen W-Y (2025) Mechanisms and targeted treatments of cobalt-encephalopathy from cobalt-chromium orthopedic implants. Neuroscience 584:32–47
114. Yagi-Utsumi M, Kato K (2022) Conformational Variability of Amyloid-β and the Morphological Diversity of Its Aggregates. Molecules 27:4787
115. Sonar K, Mancera RL (2022) Characterization of the Conformations of Amyloid Beta 42 in Solution That May Mediate Its Initial Hydrophobic Aggregation. J Phys Chem B 126:7916–7933
116. Irving H, Williams RJ (1953) P. The stability of transition-metal complexes. J Chem Soc 3192–3210
117. Wallin C et al (2016) Characterization of Mn(II) ion binding to the amyloid-beta peptide in Alzheimer's disease. J Trace Elem Med Biol 38:183–193

118. Berntsson E et al (2023) Residue-specific binding of Ni(II) ions influences the structure and aggregation of amyloid beta (Abeta) peptides. Sci Rep 13:3341
119. Alies B et al (2013) Cu(II) affinity for the Alzheimer's peptide: tyrosine fluorescence studies revisited. Anal Chem 85:1501–1508
120. Brylinski M, Skolnick J (2011) FINDSITE-metal: integrating evolutionary information and machine learning for structure-based metal-binding site prediction at the proteome level. Proteins 79:735–751
121. Cao X et al (2017) Identification of metal ion binding sites based on amino acid sequences. PLoS ONE 12:e0183756
122. Peana M et al (2013) Manganese and cobalt binding in a multi-histidinic fragment. Dalton Trans 42:16293–16301
123. Pearce DA, Sherman F (1999) Toxicity of copper, cobalt, and nickel salts is dependent on histidine metabolism in the yeast Saccharomyces cerevisiae. J Bacteriol 181:4774–4779
124. Faller P, Hureau C (2009) Bioinorganic chemistry of copper and zinc ions coordinated to amyloid-β peptide. Dalton Trans 1080–1094. 10.1039/B813398K
125. Bousejra-ElGarah F, Bijani C, Coppel Y, Faller P, Hureau C (2011) Iron(II) Binding to Amyloid-β, the Alzheimer's Peptide. Inorg Chem 50:9024–9030
126. Wallin C et al (2020) Metal ion coordination delays amyloid-beta peptide self-assembly by forming an aggregation-inert complex. J Biol Chem 295:7224–7234
127. Abelein A, Gräslund A, Danielsson J (2015) Zinc as chaperone-mimicking agent for retardation of amyloid β peptide fibril formation. *Proc. Natl. Acad. Sci. U. S. A.* 112, 5407–5412
128. Brännström K, Öhman A, Lindhagen-Persson M, Olofsson A (2013) Ca(2+) enhances Abeta polymerization rate and fibrillar stability in a dynamic manner. Biochem J 450:189–197
129. Al-Hilaly YK et al (2013) A central role for dityrosine crosslinking of Amyloid-β in Alzheimer's disease. Acta Neuropathol Commun 1:83
130. Roy RG, Mandal PK, Maroon JC (2023) Oxidative Stress Occurs Prior to Amyloid Aβ Plaque Formation and Tau Phosphorylation in Alzheimer's Disease: Role of Glutathione and Metal Ions. ACS Chem Neurosci 14:2944–2954
131. Calvo-Rodriguez M et al (2024) Real-time imaging of mitochondrial redox reveals increased mitochondrial oxidative stress associated with amyloid β aggregates in vivo in a mouse model of Alzheimer's disease. Mol Neurodegener 19:6
132. Huang Y et al (2025) Evaluation of increased oxidative stress in the brain of patients with early Alzheimer's disease by 64Cu-ATSM PET/MRI. J Neural Transm. https://doi.org/10.1007/s00702-025-03081-0
133. Berntsson E et al (2023) Characterization of Uranyl (UO(2)(2+)) Ion Binding to Amyloid Beta (Abeta) Peptides: Effects on Abeta Structure and Aggregation. ACS Chem Neurosci 14:2618–2633
134. Hedberg YS et al (2019) Synergistic effects of metal-induced aggregation of human serum albumin. Colloids Surf B Biointerfaces 173:751–758

135. Richter-Bisson ZW, Doktor A, Hedberg YS (2023) Serum Albumin Aggregation Facilitated by Cobalt and Chromium Metal Ions. ACS Appl Bio Mater 6:3832–3841
136. Sharma SK, Goloubinoff P, Christen P (2008) Heavy metal ions are potent inhibitors of protein folding. Biochem Biophys Res Commun 372:341–345
137. Tamas MJ, Sharma SK, Ibstedt S, Jacobson T, Christen P (2014) Heavy metals and metalloids as a cause for protein misfolding and aggregation. Biomolecules 4:252–267
138. Zheng F et al (2021) Cobalt induces neurodegenerative damages through Pin1 inactivation in mice and human neuroglioma cells. J Hazard Mater 419:126378
139. Tang J et al (2023) Cobalt induces neurodegenerative damages through impairing autophagic flux by activating hypoxia-inducible factor-1α triggered ROS overproduction. Sci Total Environ 857:159432

Figures

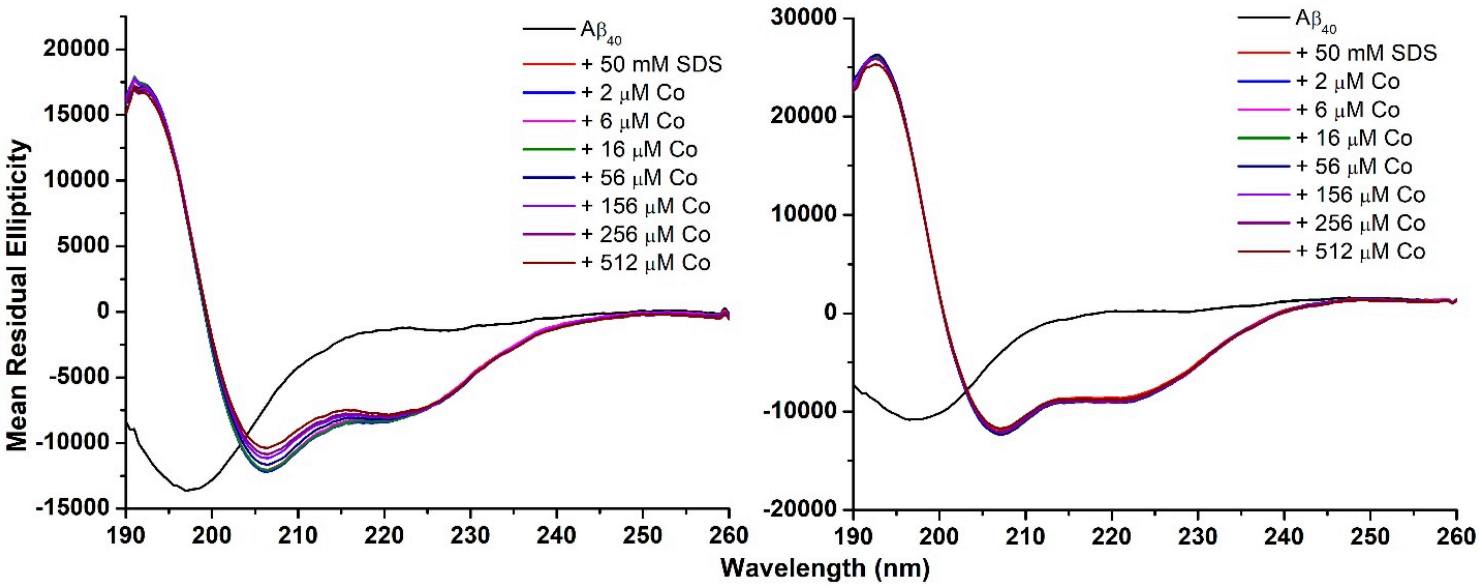


Figure 1

CD spectra of 10 μM Aβ peptide in 20 mM phosphate buffer, pH 7.3 at 20 °C. **A:** $A\beta_{40}$. **B:** $A\beta_{NoHis}$. First, spectra were recorded of Aβ in buffer only (black), then 50 mM SDS was added (red). Finally, aliquots of $CoCl_2$ were added in different steps: 2 μM (blue); 6 μM (magenta); 16 μM (green), 56 μM (dark blue), 156 μM (violet), 256 μM (purple) and 512 μM (brown).

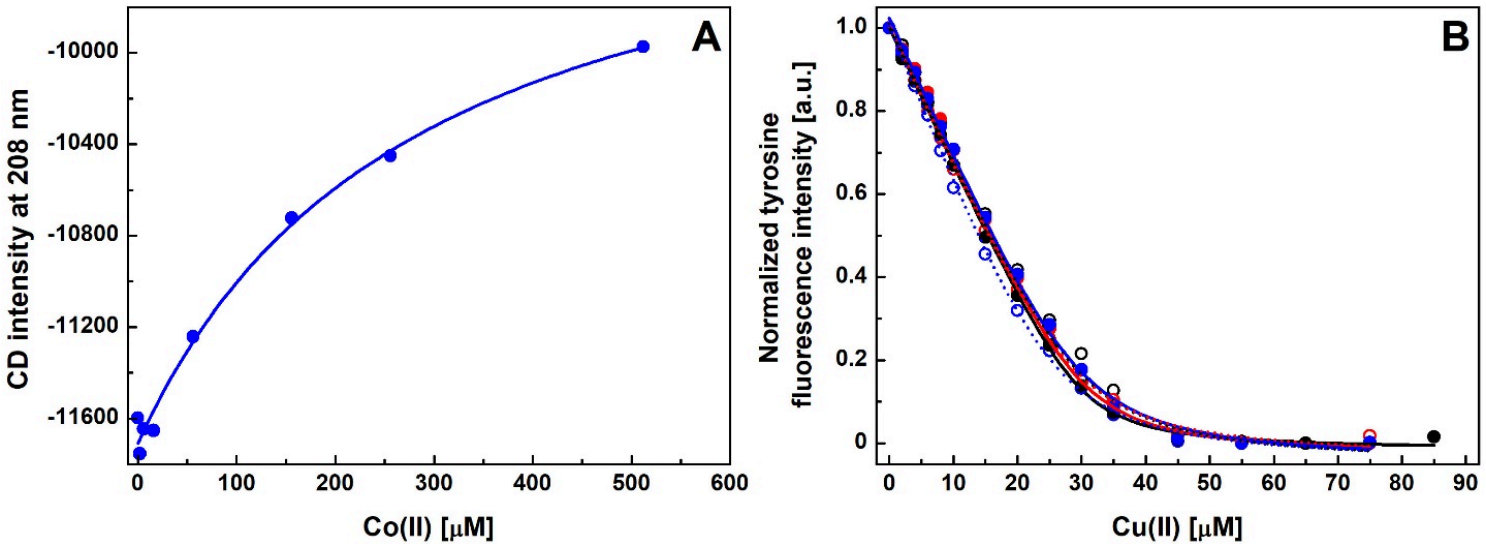


Figure 2

A: Binding curve for Co(II) binding to $A\beta_{40}$, obtained by plotting CD intensities at 208 nm from Fig. 1A (Table 1) versus Co(II) concentration. **B:** Fluorescence quenching binding curves for additions of Cu(II) to 10 μM $A\beta_{40}$ in 20 mM MES buffer, pH 7.3 at 25 °C, recorded both without (hollow circles and dotted lines) and with (filled circles and solid lines) 50 μM $CoCl_2$ being present in the sample. Three replicates of each condition were recorded, shown in blue, red and black.

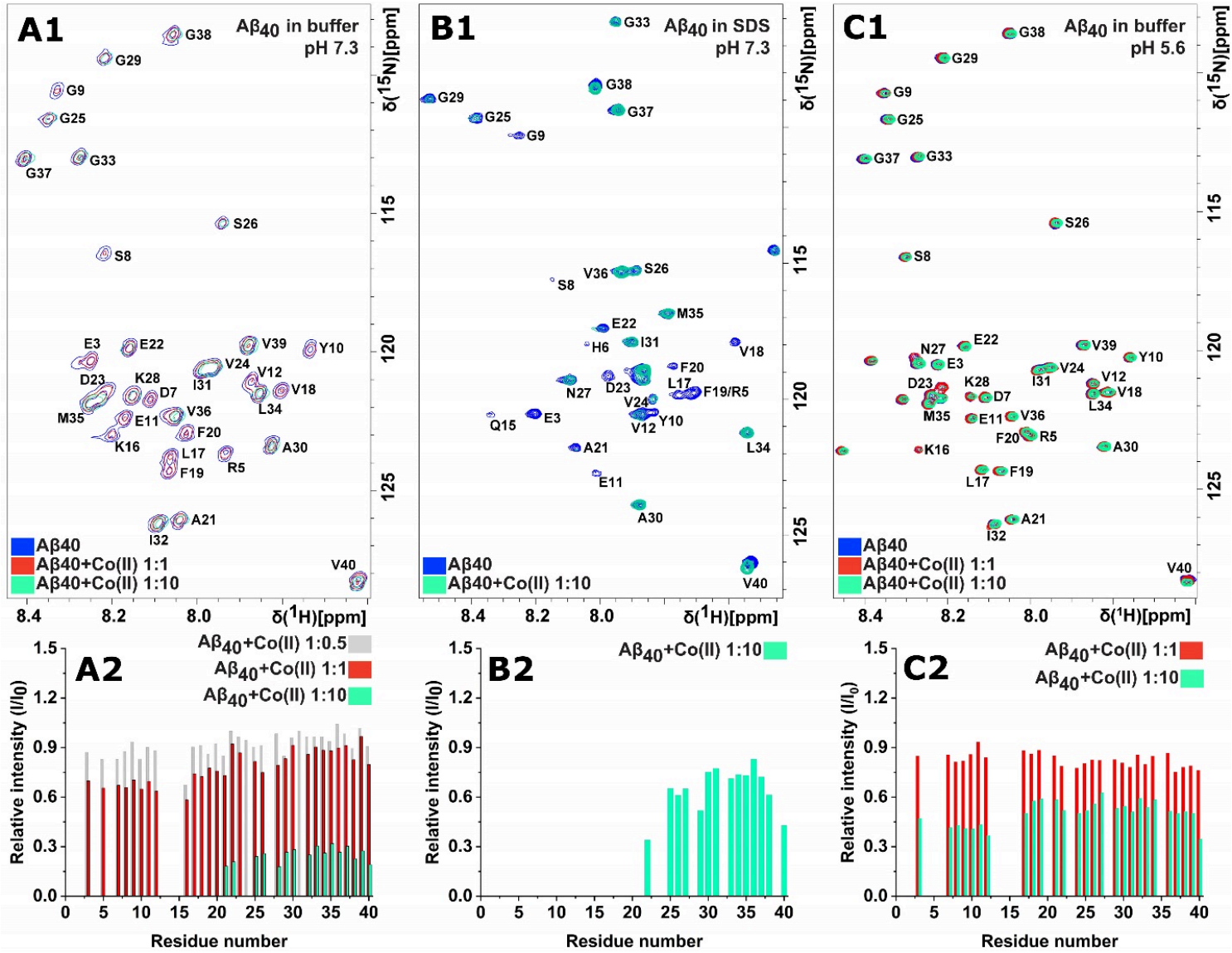


Figure 3

2D NMR $^{1}H,^{15}N$-HSQC-spectra of 84 µM ^{15}N-labeled $A\beta_{40}$ at 5 °C in 20 mM phosphate buffer (blue) and after addition of 42 µM $CoCl_2$ (grey), 84 µM $CoCl_2$ (red), and 840 µM $CoCl_2$ (turquoise), respectively. The upper row shows the NMR spectra, while the lower row shows the relative intensities of the $A\beta_{40}$ residue crosspeaks calculated from the NMR spectra. Panel A: pH 7.3; Panel B: pH 7.3 with 50 mM SDS detergent; Panel C: pH 5.6.

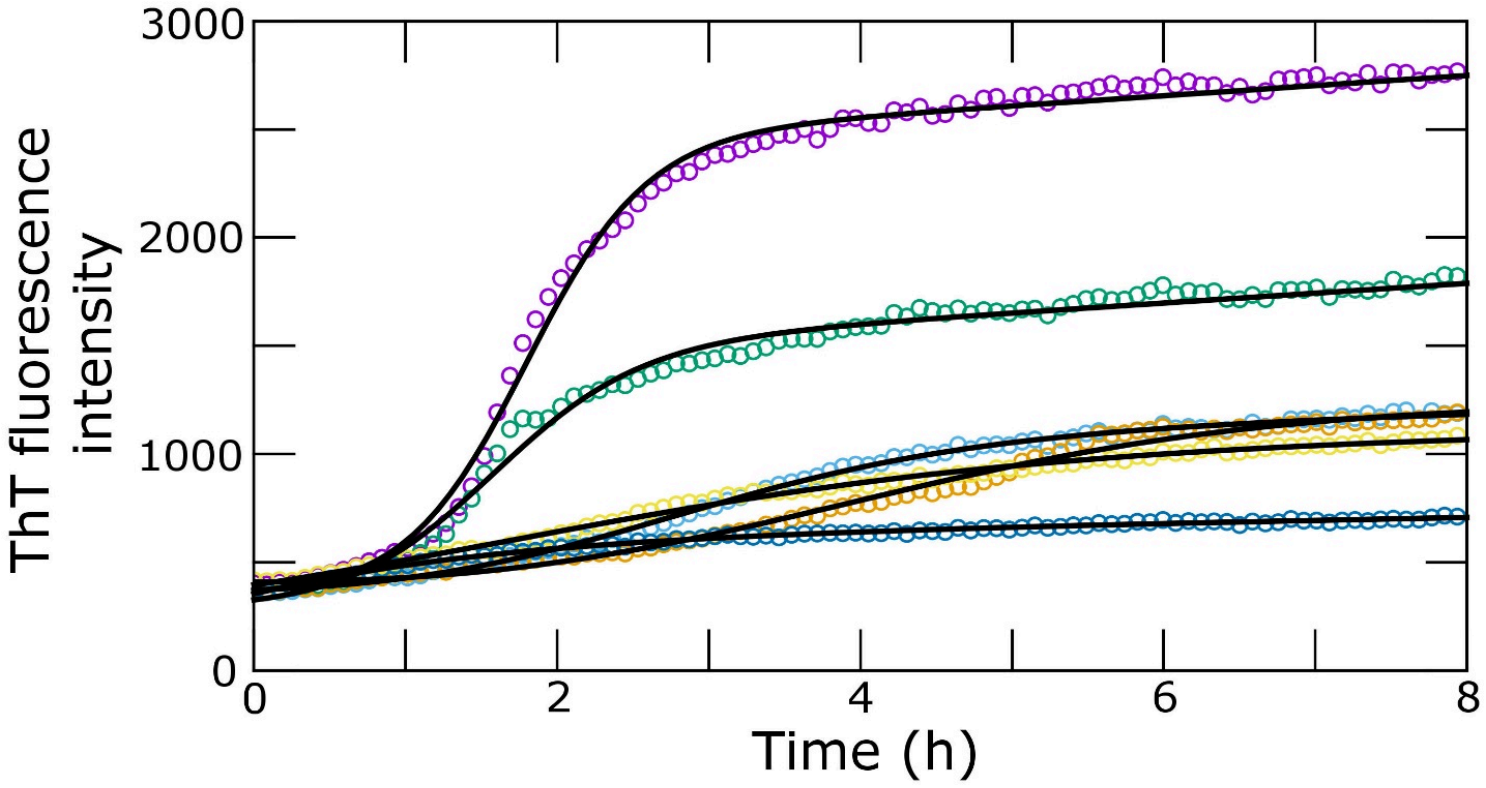


Figure 4

Kinetics of amyloid fibril formation monitored by ThT fluorescence. Samples of 10 μM $A\beta_{40}$ and 20 μM ThT dye in 20 mM MES buffer, pH 7.3, and varying $CoCl_2$ concentrations were incubated at 37 °C and shaking at 200 rpm for 15 hrs. Purple - zero $CoCl_2$ (control); Green - 0.5 μM $CoCl_2$; Light blue - 2 μM $CoCl_2$; Orange - 5 μM $CoCl_2$; Yellow - 20 μM $CoCl_2$; Dark blue - 200 μM $CoCl_2$.

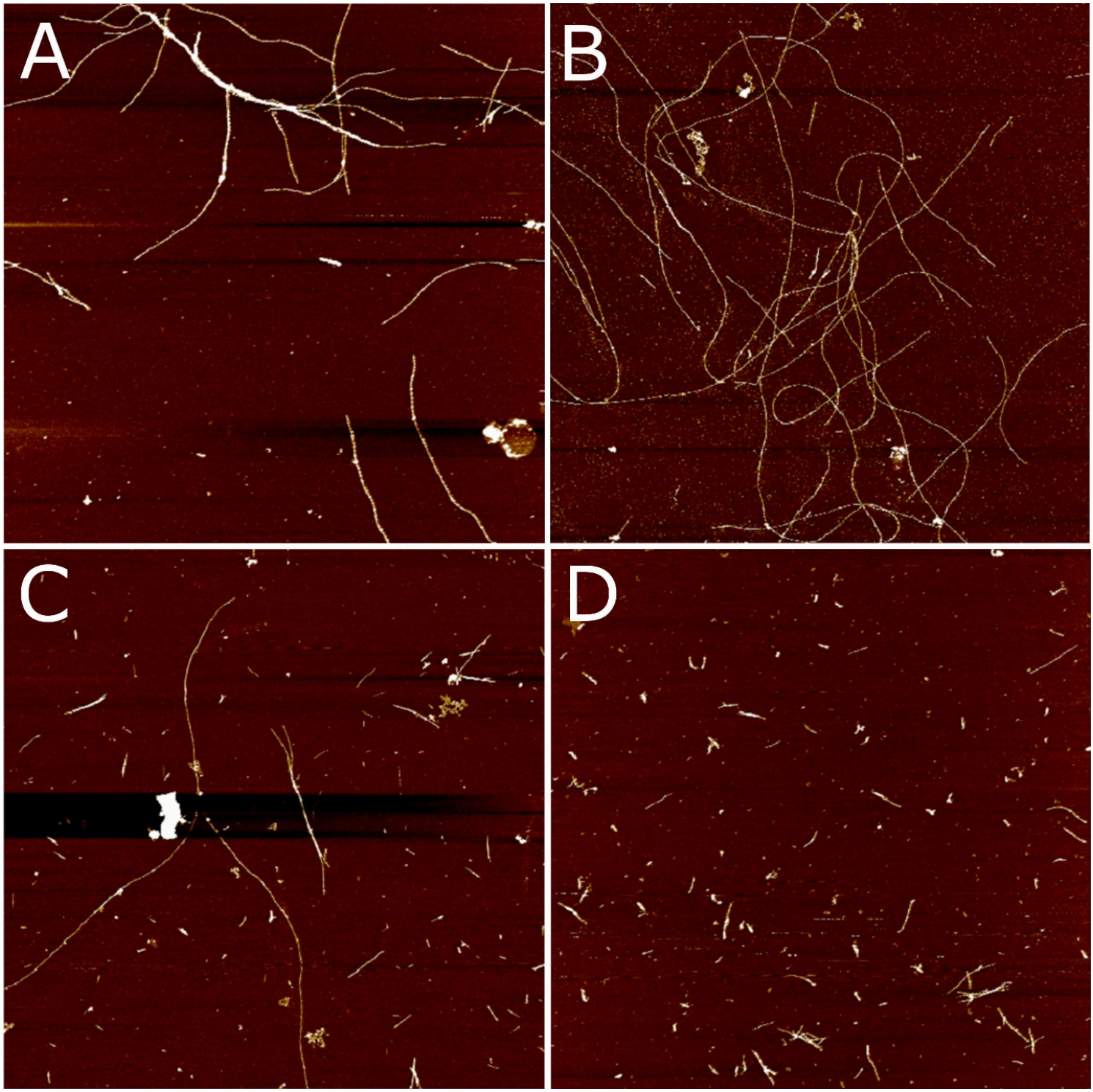


Figure 5

AFM images of aggregated 10 μM $A\beta_{40}$ peptide, incubated for 24 hrs in 10 mM sodium phosphate buffer, pH 7.3, together with different concentrations of Co(II) ions. A. zero μm $CoCl_2$; B. 1 μm $CoCl_2$; C. 10 μm $CoCl_2$; D. 50 μm $CoCl_2$. The scan size is 15 x 15 μm. Images recorded by JP.